EFDA–JET–PR(09)01

T. Craciunescu, G. Bonheure, V. Kiptily, A. Murari, I. Tiseanu, V. Zoita
and JET EFDA contributors

A Comparison of Four Reconstruction Methods for JET Neutron and Gamma Tomography

A Comparison of Four Reconstruction Methods for JET Neutron and Gamma Tomography

T. Craciunescu[1], G. Bonheure[2], V. Kiptily[3], A. Murari[4], I. Tiseanu[1], V. Zoita[1]
and JET EFDA contributorss*

JET-EFDA, Culham Science Centre, OX14 3DB, Abingdon, UK

[1]EURATOM-MEdC Association, National Institute for Laser, Plasma and Radiation Physics, Bucharest, Romania
[2]Partners in the TEC , 'Euratom-Belgian state' Association LPP-ERM/KMS, B 1000 Brussels, Belgium
[3]EURATOM/UKAEA Association, Culham Science Centre, Abingdon, Oxon, UK
[4]Consorzio RFX, Associazione ENEA-Euratom per la Fusione, Padova, Italy
** See annex of F. Romanelli et al, "Overview of JET Results",*
(Proc. 22 [nd] IAEA Fusion Energy Conference, Geneva, Switzerland (2008)).

Preprint of Paper to be submitted for publication in
Nuclear Instruments and Methods in Physics Research Section A

ABSTRACT.
The JET neutron profile monitor coverage of the neutron/gamma emissive region enables tomographic reconstruction. However, due to the availability of only two projection angles and to the coarse sampling, tomography is a highly limited data set problem. A comparative study concerning the applicability to JET tomography of four methods– maximum likelihood, maximum entropy, Tikhonov regularization and a Monte Carlo back-projection algorithm - is reported. The methods have been tested on numerically simulated phantoms with shapes characteristic for this kind of tomography. The retrieval of sophisticated structures in the emissive distribution has been addressed in order to have a complete image of the quality and reliability of the methods. A both qualitative and quantitative evaluation is reported.

1. INTRODUCTION

JET neutron profile monitor is a unique instrument among neutron diagnostics available at large fusion research facilities [1-3]. The profile monitor comprises two fan shaped multi-collimator cameras, with 10 channels in the horizontal camera and 9 channels in the vertical camera. Neighbour channels are 15-20 cm apart and have a 7cm width as they pass near the plasma centre. A schematic drawing of the JET neutron emission profile monitor, showing the 19 lines of sight, is presented in Fig.1. Each line of sight is equipped with a set of three different detectors: i) a NE213 liquid organic scintillator with Pulse Shape Discrimination (PSD) electronics for simultaneous measurements of the 2.5MeV D-D neutrons, 14MeV D-T neutrons and γ Reach detector is equipped with a pair of pulse shape discriminators, one tuned for D-D neutrons and the other one for D-T neutrons, to distinguish neutrons from γ ray induced events; the upper and lower energy detection biases are set to detect preferentially unscattered neutrons and to reject scattered neutrons. ii) a BC418 plastic scintillator, insensitive to $E\gamma < 10$MeV for the measurements of 14MeV D-T neutrons; different detection thresholds can be set for the proton recoil energy in order to obtain different sensitivity to the scattered neutrons; iii) a CsI(Tl) scintillation detector for measuring the hard X-rays and gamma emission in the range between 0.2 and 6 MeV. The collimation can be adjusted by use of two pairs of rotatable steel cylinders. The size of the collimation can modify the count rates in the detectors by a factor of 20. The instrument has currently a time resolution of 10ms.

The plasma coverage determined by the 19 lines of sight can be used for neutron or γ-ray tomography. It ensures a 2D arrangement for measurements and distribution determination. The 2D slice is located in the plane defined by the major torus radius (R) and the major torus axis (Z). The thickness of the plasma slice along the toroidal direction, determined by the collimation system, is approximately 75 mm. However, the existence of only two views (projections in tomographic terms) and the coarse sampling in each projection leads to a highly limited data set tomographic problem. For example, in the case of a reconstruction grid with 20×35 pixels (pixel size of 90×90mm) an image with 700 pixel values must be retrieved from 19 experimental data. As a consequence, special algorithms which are suitable and specific to the machine and its constrains, allowing effective tomography from the available limited data, must be developed.

A number of valuable approaches were developed in the past for tomographic reconstruction of the two-dimensional 2-D neutron and gamma emissivity at JET. A hybrid pixel/analytic algorithm, which involves a poloidal Fourier analysis and a radial Abel inversion, starting from outside and working inward is reported in Ref.4. Ingesson et al. [5] applied for γ-ray [6-8] and neutron [9-12] tomography, a constrained optimization method that was used previously for X-ray and bolometer measurements at JET. As this method uses anisotropic smoothness on flux surfaces as objective function and measurements as constraints, it searches for the emissivity distribution that is constant on flux surfaces and gently varying in the radial direction. The applicability of the minimum Fisher regularization tomographic method [13], was also extended from soft X-ray and bolometric data to neutron tomography [14, 15]. In principle, the Fisher information of the unknown 2-D distribution is minimized, while the measurements are taken into account as constraints, using Lagrangian multipliers. Recently, it was proved that tomography based on the maximum likelihood principle provides good reconstructions in terms of shapes and resolution [16]. The method uses a smoothing operator, defined as median filtering along the magnetic contour lines.

Several other methods were reported in literature for various fusion studies. Among them, most widely used are the Maximum Entropy (ME) and the Tikhonov Type Regularization (TR). ME has been actively discussed in the literature in connection with the problem of obtaining the most probable solution with incomplete data [17−19]. ME was first applied for tomography by Minerbo [20]. In case of tomography for fusion studies, contradictory results were reported. A moderate quality of the reconstruction was reported for reconstruction geometries characterized by several non-uniformly distributed projections around the plasma [13, 21], with an exception [22]. On the contrary, good results were reported for reconstruction geometries with two projection angles and simple emmisivity shapes (peak, hollow) [23, 24]. The Tikhonov regularization was also used for numerically stabilizing the ill-conditioned plasma image reconstruction. [21, 25]. The objective function to be minimized lead to a linear estimator of the image intensity. The linear regularization smoothes the solution in addition to providing a reasonable fit to data.

The aim of this paper is to enlarge the variety of tomographic methods tested for JET neutron and gamma tomography. It reports the comparison of four tomographic reconstruction techniques. The maximum entropy method and an implementation of the Tikhonov regularization technique for tomographic reconstruction are introduced together with the recently developed method based on the maximum likelihood principle. A Monte Carlo Back−Projection (MCBP) technique, that proved to provide good results in limited data tomography [26, 27] has also been considered for this study. The methods are tested on numerically simulated phantoms with shapes characteristic for this kind of tomography. The retrieval of sophisticated structure in the emissive distribution was addressed in order to have a complete image of the quality and reliability of the methods. A both qualitative and quantitative evaluation is reported.

2. METHODS

In 2-D tomography systems, measurements are taken along lines of sight and can essentially be represented by line integrals; i.e. the measurement p is given by straight line integrals of the emissivity $f(x, y)$, where x and y are Cartesian coordinates of the plane. The emissivity function can be appropriately discretized on a 2-D grid. For this purpose, the reconstruction area is divided into pixels that are sufficiently small for emissivity variations within a pixel to be negligible. The weight matrix W describes the geometrical layout of the detectors and its element w_{ik} indicates the contribution of the i*th* pixel to the k*th* detector.

The basic set of tomographic equations is:

$$p_k = (\sum_{i=1}^{n_P} w_{ij} \cdot f_j,\ k = 1, 2 \ldots, N_d \tag{1}$$

where N_p and N_d are the numbers of pixels and detectors, respectively. This set of linear equations represents the linear inverse problem. Obviously, even with exact data constraints, this inversion cannot be uniquely performed when there are fewer data than pixels, as is generally the case in plasma tomography.

As the tomographic problem is highly undetermined, the reconstruction algorithm can lead to a solution which satisfy Eq. 1 but has no physical relevance and may bring about wrong interpretations. A priori information about the expected emission profile can be introduced in order to compensate for the lack of experimental information. Smoothness can be imposed on the solution of the tomographic problem as regularization. In order to prevent oversmoothing which may lead to the blurring of certain features in the reconstruction, it is necessary to find the smoothest function for which the misfit is equal to the estimated noise.

Referece [5] introduced an anisotropic diffusion-like smoothness function as a term in the objective function of the tomographic problem, formulated as a regularization factor. It takes into account that the emission profile is smoother in the poloidal direction than in the radial one. Using measurements as constraints, the reconstruction method searches for the emissivity distribution that is constant on flux surfaces and gently varying in the radial direction. The functional used to quantify the global unsmoothness of the solution is formulated by a scalar product ([7], Appendix C):

$$\langle f|\Omega|f\rangle = \sum_i \left\{ a_0 f_i^2 + \left[a_x \left(\frac{f}{\partial x}\right)^2 + a_y \left(\frac{f}{\partial y}\right)^2 \right]_i + \left[a_{xx} \left(\frac{^2f}{\partial x^2}\right)^2 + a_{xy} \left(\frac{^2f}{\partial x \partial y}\right)^2 + a_{xx} \left(\frac{^2f}{\partial y^2}\right)^2 \right]_i \right\} \tag{2}$$

where Ω is the unsmoothness operator. The a_0 term penalizes large values of $f(x, y)$. The first derivative terms force the solution to be as flat as possible, whereas the second derivative terms force it to be as smooth as possible.

Smoothness on flux surfaces is assumed also in [16]. The smoothing operator is implemented as one-dimensional median filtering, using a sliding window which moves on the magnetic contour lines:

$$f_i^{smooth} = \sum_{\substack{j=-w_{med} \\ w_{med} \in L_k}}^{j=+w_{med}} m_{ji} f_j \tag{3}$$

where m_{ji} is the matrix which defines the window-based median filter, w_{med} is half of the width of filtering window and L_k designates a close magnetic contour line L_k. The smoothing operator does not need to be integrated in the objective function of the tomographic problem. It works directly on the reconstructed image, at different stages of the reconstruction process. This technique was an appropriate choice for this work, which deals with a variety of methods with different algorithmic formulations.

Additional smoothing can be obtained by resampling the experimental projection. Projection resampling implies the introducing of virtual lines of sight which ensures an improved coverage of the reconstruction domain. Spline interpolation was used for resampling implementation. The combination of median filtering along magnetic contour lines and projection resampling is strong enough to allow neglecting the beam-width when calculating the elements of the weighting matrix W.

2.2 MAXIMUM LIKELIHOOD

Bayesian statistics represents an appropriate framework for introducing the ML method. Bayesian inference provides a numerical measure of the probability of some event with consistent consideration for prior information. Bayes' theorem supplies the rule for determining the posterior probability:

$$P(f, \mid p, z) = P(p, \mid f, z)\, \frac{P(f \mid z)}{P(p \mid z)} \tag{4}$$

Where f is a particular solution in view of experimental data p and additional parameters z (e.g. error bars). $P(p|f,z)$ quantifies the probability of measuring data p if a reconstruction f and parameters z are given. It represents the likelihood function, which contains the new information provided by the experiment. According to Bayes' theorem, the likelihood has to be blended with the prior probability $P(p|f,z)$ based on the information z prior to any experiment - of getting the posterior probability distribution. $P(p|f,z)$ is not related to the maximal value of $P(p|f,z)$ and so will be treated as a constant for the present purpose. The most trustworthy reconstruction is that which maximizes the probability distribution $P(p|f,z)$ (see Eq. (4)).

If there is no a priori source information available, $P(p|f,z)$ can be assumed as constant, implying that all possible source distribution are equally likely, therefore maximizing the Bayesian results in the same way as maximum likelihood. In tomography problems, the likelihood probability density function follows the error statistics of the experimental data. If it is assumed that each projection ray p obeys Poisson statistics, with all of them statistically uncorrelated, the likelihood function $P(p|f,z)$ has the form:

$$P(p|, f,) = \prod_k \left[\frac{1}{p_k!} \left(\sum_i w_{ik} f_i \right)^{p_k} \times exp\left(- \sum_i w_{ik} f_i \right) \right] \tag{5}$$

An efficient iterative solution of this nonlinear optimization problem was given in Refs. 28-29:

$$f_i^{(iter+1)} = f_i^{(iter)} \frac{\sum_k w_{ik} \frac{p_k}{\sum_l w_{jl} f_j^{(iter)}}}{\sum_l w_{ik}} \tag{6}$$

where $f_i^{(iter)}$ is the reconstructed image for the iteration *iter*, *i* and *j* are image element indices, and are projection element indices. The iterative ML algorithm (Eq.6) works directly on the reconstructed image which is successively updated. This allows image manipulation at each iteration for introducing *a priori* knowledge. Therefore smoothing is applied, as described, at each iteration.

2.3 MAXIMUM ENTROPY

The Maximum Entropy (ME) has become a common regularization method and a widely adopted way to overcome the indeterminacy of ill-posed problems. ME can be derived starting also from the Bayes formula (4), by a different choice of the prior probability $P(p|f,z)$ and also of the likelihood function $P(p|f,z)$.

The total lack of information about the emissive source assumed in the case of ML method is replaced by the simplest expert knowledge: the emissivity distribution have to be positive. Thus, within the Bayesian approach, this expert knowledge enters the analysis as prior distribution and contributes to the shape of the posterior distribution. On the basis of information theory, Skilling [30] have shown that the most uninformative and most unbiased prior is the entropic prior:

$$P(p|, f, z) = \frac{\alpha}{2\pi}^{n_p 2} \; exp(\alpha S) \tag{7}$$

where:

$$S = \sum_i^{N_P} \left[f_i - m_i - f_i \, 1\mathrm{n} \left(\frac{f_i}{m_i} \right) \right] \tag{8}$$

is the entropy relative to the default model *m* and α is a positive constant. The default model *m* is that reconstruction where the entropy and the prior have their maximum, and to which *f* would default in the absence of any data. Possible prior information about the structure of the solution can be encoded in the default model. However, the usual approach is to consider complete prior ignorance, which means a flat distribution for *m* ($m_i = const$). The entropic prior is a positive and additive distribution function.

The probability of obtaining a certain signal $P(p|f,z)$, with *f* given, is defined by the error statistics appropriate to the respective experimental problem. Most of the data $\{p(f)\}$calculated with the forward transform (Eq.1) from the manifold of conceivable sets $\{f\}$ are very different from the data *p* actually observed. The 'misfit' is characterized by the parameter χ^2. For uncorrelated noise η of the detector signals and Gaussian distribution with variance σ_i, the likelihood function - the product of the likelihoods of each observation *p* – becomes:

$$P\,(p|\,f,\,z) \propto \exp\left(-\frac{1}{2}\,\chi^2\right) \tag{9}$$

where:

$$\chi^2 = \sum_i^{N_d} \left(\frac{p_i - p_i(f)}{\sigma_i}\right)^2 \tag{10}$$

Provided α is known, the reconstruction with the largest posterior probability (Eq.(4)) corresponds to the maximum of

$$\Psi(\alpha, f) = \alpha \cdot S - \frac{1}{2}\,\chi^2 \tag{11}$$

α can be interpreted as a regularization parameter which controls the balance between prior information (default model), represented by the entropy term, and data constraints, represented by the misfit parameter χ^2.

The maximization of Ψ with respect to can be obtained introducing Lagrangean multipliers which strongly reduce the computational effort. We used the procedure described in Ref.31. The space of the variables is enlarged to $[f_i\,|\,i=1,2,...,N_p\}\cup\{P_i\,|\,k=1,2,...,N_d\}$ but the number of unknowns is reduced from N_p to N_d. The equation:

$$\Psi(\alpha, f, p) = \alpha S - \frac{1}{2}\sum_k \frac{(p_k - P_k)^2}{\sigma_k^2} \tag{12}$$

subject to the constraints $P_k = p_k\,(f_k)$, is maximized. This leads to an unconstrained maximization of:

$$\tilde{\Psi}(\alpha, f, P) = \alpha S - \frac{1}{2}\sum_k \frac{(p_k - P_k)^2}{\sigma_k^2} + \alpha \sum_k \lambda_k\,[\mathrm{P}_k - p_k(k)] \tag{13}$$

with respect to f, P and λ. Maximizing with respect to f gives the Euler-Lagrange equation:

$$f_i = m_i \exp\left(-\sum_k w_{ik}\,\lambda_k\right) \tag{14}$$

which constitutes an N_d dimensional basis for possible reconstruction of f. The required *Lagrange parameters*, λ_k, could be found after maximizing $\tilde{\Psi}$ with respect to λ and P, which amounts to solve the nonlinear equation for l:

$$\tilde{\Psi}(\lambda) = p_k - \sum_i^{Np} I_{ki}\,m_i \exp\left(-\sum_{k'} I_{ki}\,\lambda_{k'}\right) + \alpha\sigma^2\,\lambda_k = 0 \tag{15}$$

The Jacobian $J_{kk} = \partial\Psi/\partial\lambda k$, of the expression is:

$$J_{kk'} = \alpha\sigma^2\,\delta_{//'} + \sum_k I_{ki}\,I_{k'i}\,\mathrm{f}_i \tag{16}$$

and is strictly positive. So Eq.(15) has a unique solution and can be efficiently solved by the Newton–Raphson method.

Therefore the retrieval of the unknown image f implies the maximization of expression (15) with respect with the Lagrange multipliers λ. After finding the parameters λ, the image can be obtained using Eq.(14). As the maximization do not manipulate directly the unknown image f, smoothing can be applied straightforward only at the end of the iterative process. This has a limited effect and does not improve enough the quality of the reconstruction, especially for distributions with complicated shapes. ME algorithm may produce noisy reconstruction results compared with other kinds of reconstruction algorithms due to the absence of correlation among adjacent pixels. Kim et al. [22] replaced the flat model m with the directly inverted model, obtained by inverting the weight matrix using the Singular Value Decomposition (SVD) technique. The SVD-based initial guess of the reconstruction allows the adjacent pixels to link smoothly. This technique succeeds in enhancing the reliability of the algorithm and improves the quality of the reconstruction for the a geometry with 16 projections and 192 bins in each projection. However for the JET geometry (2 projections with a total of 19 projection bins), which determines the highly indeterminacy of the tomographic problem, the directly inverted model is far from the desired solution. This may lead to a local solution during the maximization of $\tilde{\Psi}(a, f, P)$ (Eq.13). Therefore we used a multiple run procedure. We start with a flat model $m = const$. The smoothing procedure was applied after each full run of the ME algorithm (solving Eq.15). Then the reconstructed image was used, in a new run, as a default model, replacing the flat one. This procedure improves the robustness of the algorithm and the quality of the reconstruction.

2.4 TIKHONOV REGULARIZATION

The Tikhonov regularization is one of the most well-known form of regularization techniques for ill-posed problems [32]. Assuming a matricial form of Eq.1: $W \cdot f = p$, the Tikhonov regularization technique is seeking for a solution , defined as the minimizer of the following weighted combination of the residual norm $\|W \cdot f = p\|^2$ and the 2-norm $\|L(f)\|^2$, where the matrix L is typically either the identity matrix I or a discrete approximation of the derivative operator (usually the first or second order derivative operator):

$$\Psi(f) = \|W \cdot f - p\|^2 + \lambda \cdot \|L(f)\|^2 = MIN \tag{17}$$

λ is a regularization parameter. λ controls the weight given to minimization of the side constraint relative to minimization of the residual norm; λ also controls the sensitivity of the regularized solution I to perturbations in W and p, and the perturbation bound is proportional to λ^{-1}.

Several choices of the operator L were reported. Second order linear regularization $L = \nabla^2$, where ∇^2 is the Laplacian operator in two dimensions, is reviewed in [25]. The gradient is minimized if first order linear regularization is chosen [21] $L(f) = \|f_x'\|^2 + \|f_x'\|^2$ (where f_x' and f_y' are the partial

derivatives with respect to x and y. $L(f) = \sum_i \frac{(f_i')^2}{f_i}$ in case of Fisher information reconstruction algorithm [13], which can be viewed as belonging also to the class of Tikhonov regularization methods. The minimization of $\|L(f)\|_2^2$ introduces different intrinsic smoothing principle in the algorithm, depending on the particular choice of L • $\|L(f)\|^2$ control the smoothness of the regularized solution, depending on the particular choice of *L*. Second order regularization selects the solution with least curvature. First order regularization minimizes the roughness of the reconstruction. Minimum Fisher information is essentially a smoothening principle just like linear regularization. The low value regions of *f* are more strongly smoothed, whereas smoothing is less pronounced where *f* is high and therefore more reliable. In our approach we used *L=I*, where I is the identity matrix. Therefore the norm of the solution is minimized together with the residual norm (Eq.17). The smoothing effect is the one typically associated with a square integrable kernel. However, this intrinsic smoothing, not connected with the magnetic information, is insufficient to avoid global distortions in the reconstruction, generated by the limited experimental information. Therefore we used additional smoothing - median filtering smoothing on flux surfaces and projection resampling - as described previously.

For solving (17) we used the method based on filter factors and the Singular Value Decomposition (SVD). The method can be briefly described as follows. The general solution f_{reg} of the regularization problem can be written in the form [33]:

$$f = \sum_i \eta_i \frac{u_i^T p}{s_i} v_i, \qquad \text{where } W = USV^T = \sum_k u_k s_k v_k^T \tag{18}$$

and η_i are filter factors for the particular regularization method. The filter factors must have the important property that as s_i decreases, the corresponding η_i tends to zero in such a way that the contributions $(u_i^T p/s_i) f_i$ to the solution from the smaller s_i are effectively filtered out [34]. Otherwise the solution is dominated by the terms in the sum corresponding to the smallest s_i. As a consequence, the solution has many sign changes and thus appears completely random. The difference between the various regularization methods lies essentially in the way that these filter factors η_i are defined. It can be shown that for Tikhonov regularization with *L=I* filter factors are:

$$\eta_i = \frac{s_i}{(s_i^2 + \lambda^2)} \tag{19}$$

and the filtering effectively sets in for $s_i < \lambda$.

The algorithm is complete if a method for choosing the regularization parameter λ is defined. The Generalized Cross-Validation (GCV) [35], is‘used in [25]. GCV is based on the philosophy that if an arbitrary element p_k in Eq.1 is left out, then the corresponding regularized solution should predict this observation well. The mean-square-error in “predicting” the *k*-th projection p_k from the estimate $f^{(k,\lambda)}$ obtained from the data excepting p_k and regularization parameter λ, can be used to obtain an optimal value for λ. Taking into account that, in our case, the total amount of experimental

data consists of only 19 projection values, GCV seems not to be appropriate for JET geometry.

A usual and convenient alternative tool to optimally set the value of the regularization parameter λ is the so-called *L-curve*. The *L*-curve is a plot - for all valid regularization parameters λ– of $\|L(f)\|^2$ versus the corresponding residual norm $\|W \cdot f = p\|$ (see e.g. [36]). For discrete ill-posed problems it turns out that the L-curve, when plotted in *log-log scale*, almost always has a characteristic L-shaped appearance (hence its name) with a distinct corner separating the vertical and the horizontal parts of the curve. It can be proved [37] that an optimal choice of the regularization parameter corresponds to the L-curve's corner. Unfortunately, due to the high degree ill posed character of the JET tomographic problem, in a number of cases, the *L*-curve has a concave appearance and consequently, a corner cannot be defined. In such cases the choice of the regularization parameter was based on the the discrepancy principle [38] which amounts to choosing the regularization parameter such that the residual norm for the regularized solution satisfies:

$$\|W \cdot f - p\| = \|\eta\| \tag{20}$$

where is a good estimation of the noise accompanying the experimental data. An underestimate of $\|\eta\|$ is likely to produce an under-regularized solution with a very large norm while, on the other hand, an overestimate produces an over-regularized solution with too large regularization error.

2.5 MONTE CARLO BACK-PROJECTION TECHNIQUE

This algorithm starts from an empty image $f_i = 0$. Then, mathematically "grains" of fixed intensities are randomly allocated. The *l-th* grain is accepted in pixel and therefore f_i is increased with the quantity *do* if, for all corresponding projections p_k, the following inequality is valid:

$$p_k - (f_i - do) = w_{ik} \quad 0 \tag{21}$$

The restored object is built up by such successive successful allocations. In order to generate the position where we try to allocate the grain, for the two available projections, $p^{horiz}_{k\{k=1..10\}}$ and $p^{vert}_{k\{k=11..19\}}$ two random numbers, k^{horiz} and k^{vert}, respectively, are generated. These two numbers select two projection rays and their intersection defines the point where we attempt to allocate the grain. A uniform generation of k^{horiz} and k^{vert} has no connection with the experimental available data. So it is more efficient to generate the two random numbers using $p^{horiz}_{k\{k=1..10\}}$ and $p^{vert}_{k\{k=1..10\}}$ as probability distribution functions. k^{horiz} and k^{vert} will be distributed preferentially where the cumulative sum $cumsum = \sum_k p_k$ has a higher slope and p_k reaches a local maximum. The generation of grain position by a procedure sensitive to the experimental data increases the speed of the reconstruction process. The magnitude of the quantity *do* is important for proper results. Building the image *f* with big grains will not allow the calculated projections $p_k^{calc} = \sum_i f_i w_{ik}$ to be more than a coarse approximation of the experimental projections p_k^{calc} because of residuals. Obviously, the use of small grains will increase the computation time.

3. RESULTS AND DISCUSSION

The efficiency of each method has been tested using phantoms with shapes characteristic of JET neutron/gamma tomography and representative results are presented in Fig.1. Each row corresponds to a phantom and its reconstruction - from left to right: the phantom and the ML, ME, TR, and MCBP reconstructions. The virtual magnetic contour lines used for reconstruction are superimposed on each image.

The *peak* phantom, (Fig.1 first row) has been constructed using a centred Gaussian $A \cdot \exp = \left(- \frac{x^2}{2\pi\sigma_x^2} - \frac{y^2}{2\pi\sigma_y^2} \right)$, ($\sigma_y = 2$, $\sigma_x = 4.8$ and A = 1). The *hollow* phantom (Fig.1 second row) is described by the relation:

$$ph\,(r) = \begin{cases} (x^2 + y^2)^{3/2}\,, for\ (x^2 + y^2)^{1/2} < \frac{N_{px}}{2} \\ 1 - (x^2 + y^2)^{1/2}\,, for\ \frac{N_{px}}{2} < (x^2 + y^2)^{1/2} < N_{px} \end{cases} \qquad (22)$$

where N_{px} is the number of pixels on the horizontal dimension of the reconstruction grid. These two phantoms are the most frequent distribution shapes encountered in experiments. However for a full characterization of the methods, more complicated shapes must be taken into account. Neutron emissivity profile in case of DT experiments provide several challenging shapes for tomographic reconstruction. Three such shapes were used here: "*banana", symmetrically reversed "banana"* and *peak plus "banana"*. The "*banana"* shape (Fig. 1 third row) and the *symmetrically reversed "banana"* (Fig.1 forth row) phantoms have been derived from the circular symmetrical shape of the "hollow", by cutting half of the shape. The "*banana"* phantom corresponds to an experiment where the DT-neutron emission was measured in the ohmic deuterium discharge during the off-axis injection of the T neutral beam. The *symmetrically reversed "banana"* phantom is, from the tomographic point of view, a more difficult case. The diverging lines of sight corresponding to the horizontal camera are more widely spread in the "*banana*" region on the high field side and this results in a reduced information density leading to shadow effects: there are more possibilities in this region to distribute each detector signal among different cells than in the region close to the detectors and this may result in reduced spatial resolution. For *peak plus "banana"* phantom (Fig.1 fifth row) the "*banana*" shape was distorted to a elliptical symmetrical one (the vertical dimension is twice the horizontal one) and a centred Gaussian was superimposed ($\sigma_y = 2$, $\sigma_x = 1.6$ and A = 0.18).This case corresponds also to a DT experiment, where the profile was recorded just after a T-puff, and tritons partly penetrated to the plasma core from the periphery. Virtual magnetic contour lines were simulated as concentric circles for the first four phantoms and as concentric ellipses for the *peak plus "banana"* phantom. The calculations have been performed on a 35×20 pixels reconstruction grid. To improve the quality of the displayed image, the size of images has been doubled, after reconstruction, using bilinear interpolation.

Several figures of merit were used in order to complete the qualitative evaluation of the quality of the reconstruction with a quantitative one.

A global evaluation of the reconstruction is given by the correlation coefficient:

$$corr = \frac{N_p^2 \sum_i f_i^{rec} f_i^{ph} - \sum_{i,j} f_i^{rec} \sum_{i,j} f_i^{ph}}{\left[N_p^2 \sum_i \left(f_i^{rec}\right)^2 - \left(\sum_i f_i^{rec} \right)^2 \right]^{\frac{1}{2}} \left[N_p^2 \sum_i \left(f_i^{ph}\right)^2 - \left(\sum_i f_i^{ph} \right)^2 \right]^{\frac{1}{2}}} \tag{23}$$

which gives a comparison between the phantom f^{ph} and the reconstruction f^{rec}. This factor has the value 1 for an ideal reconstruction. The ratio R_{emiss} between the total volume of the distribution given by the tomographic reconstruction method and the total volume of the phantom, may assess the correctness of the total emissivity reconstruction, also by means of a single number.

Finally, also a global evaluation is given by the comparison between the initial projections $p^{(ini)}$ and the calculated ones $p^{(calc)}$; projections $p^{(ini)}$ were calculated using Eq.1, where f is the phantom; projections $p^{(calc)}$ were calculated using the same equation, but in this case f represents the reconstruction. This comparison must be taken into account cautiously. For a good reconstruction a good agreement must exists between $p^{(ini)}$ and $p^{(calc)}$. However, since a limited set of projections is available, a good agreement does not guarantee necessarily a good reconstruction.

The assessment of the spatial resolution can be obtained by means of line profiles. The horizontal and vertical line profiles describe the image intensity variation along the horizontal and vertical axes of a coordinate system with the origin in the centre of the image. The main image features, for all the phantoms, intersect these two axes. Information about the quality of the shape and size reconstruction is given by line integrals, calculated along the magnetic contour lines, starting from the centre of the reconstruction and covering the whole image.

The values obtained for the correlation coefficient *corr* and the ratio R_{emiss} describing the reconstruction of the total emissivity are given in Table 1 and 2, respectively.

The other figures of merit, which allow a graphical representation, are illustrated in Fig.2 (line profiles, integrals along magnetic contour lines) and Fig.3 (phantom versus reconstruction projection). They are normalized to the maximum value. The root mean square difference *rms* of a generic figure of merit g, for each phantom $g^{(ph)}$and reconstruction $g^{(rec)}$, respectively, has been calculated using the equation:

$$rms = \sqrt{\sum_i (g_i^{(ph)} - g_i^{(rec)})^2 / N} \tag{24}$$

where N is the size of vectors $g^{(ph)}$, $g^{(rec)}$. The *rms* values are listed in Table 3.

For the *peak* phantom, the most common distribution encountered in experiments, good reconstructions are obtained using all the methods. The ML method gives the best value for the root mean square difference between projections calculated using the phantom and the reconstruction.

The TR method offers optimal results for the line profiles. The correlation coefficient and the ratio of reconstructed volumes finest results are provided by the MCBP. In fact, all the methods gives accurate results, with similar values for all factors of merit.

Similar remarks are valid also for the case of the *hollow* phantom with the exception of the MCBP method, which gives a reconstruction with lower spatial resolution. Finest results are obtained using the ML method except the ratio of reconstructed volumes for which the TR method gives the result closest to 1. It must be noticed that the ML method provides, for this distribution and also for the next ones, the most regular and symmetric shapes.

The methods give significantly different results when the symmetry of the distribution, with respect to the two axis, is reduced or eliminated. The line profiles (both horizontal and vertical), but especially the contour line integral values proves that the best results, in case of "*banana*" and *symmetrically reversed "banana"* are obtained using the ML method. As far as the other methods are concerned, it is difficult to choose between the TR and ME methods. The images show more similarity between the shapes reconstructed by the ME method and the phantoms. This is confirmed also by the values of the correlation coefficient. The images retrieved using the TR method are slightly distorted and affected by a central artefact. However, the TR method gives better values for the line profiles (both horizontal and vertical), and also for the contour line integral. But starting with the *"banana"* phantom, the TR method does not provide the best values for R_{emiss} anymore. The MCBP method is able to reproduce the "*banana*" shapes but with the same low spatial resolution.

The *peak plus "banana"* distribution is, from the tomographic point of view, the most complex and challenging structure. The only reasonable reconstruction is given by the ML method. The TR method looses spatial resolution and almost equals the MCBP method. Both methods prove unable to completely resolve the two features in the image. The ME method discriminates the two components in the image, but introduces shadow artefacts in retrieving the *"banana"* component which is also shifted and reproduced incompletely. The hierarchy of the methods is confirmed by the quality factors.

The reconstruction time is an important parameter especially if the method is intended to be used in inter-shot analysis. The methods have been implemented, as described earlier, in MATLAB and consequently, the computing time needed for reconstruction is reported, for this specific implementation, in Table 4. The TR method is the fastest one, due to its formulation which involves pure matrix manipulation. Most of the computer time needed for this method is spent on smoothing. However smoothing can not be avoided in order to obtain as correct as possible reconstruction. The ML and ME methods are iterative non-linear algorithms and consequently the computation time is one order of magnitude higher. However, the computing time needed for a ML reconstruction is still practicable for inter-shot analysis. In case of ME method, Kim et al. (see Ref. 23) reported that the algorithm can be modified in such a way that it uses simple matrix operations instead of treating a fully nonlinear problem. This may diminish the computation time and make it comparable with that of the TR method. MCBP, even it is a Monte Carlo method, due to the small scale of the problem, is able to perform image retrieval in a relatively short time

In conclusion we can say that the comparative evaluation is able to establish a clear hierarchy of the tested methods. The evaluation has been performed with phantoms. These numerically simulated emissive distributions are characteristic for JET neutron and gamma tomography. They cover most of the range of possible distributions for this kind of tomography. Simple but frequent shapes are considered together with the retrieval of sophisticated structure in the emissive distribution which proved to be essential for a complete image of the quality and reliability of the methods. The evaluation reveals that the ML method is the only one able to encompass the reconstruction, with a good quality, of all structures of the emissive distribution. The ML method provides the finest results in terms of shapes reconstruction and resolution and produces artefact free images. For the simple shapes (*peak* and *"banana"*), the total emissive volume is better retrieved by the TR method. This can be explained by means of the effects of the smoothing, which determines a blurring effect, superimposed on the image. The effect is more strong in case of the ML method where the amount of smoothing is increased: the smoothing operator is applied at each iteration, while for the TR method smoothing is applied only once, after the reconstruction. However, for more complicated shapes, the larger amount of smoothing becomes an advantage because it drives the reconstruction closer to the shapes to be recovered. For simple, but frequent experimental type of distributions (*peak*, *hollow*), all the methods provide good results. For this cases, if very fast reconstructions are needed (e.g. for a large amount of data processing), the TR method is an appropriate choice.

ACKNOWLEDGEMENT

This work was supported by the European Communities under the contract of Association between EURATOM/MEdC, and was carried out within the framework of the European expressed herein do not necessarily reflect those of the European Commission. Fusion Development Agreement. The views and opinions. Any request for permission to reuse parts of the article shall be directed to the author.

REFERENCES

[1]. J.M. Adams, O.N. Jarvis, G. J. Sadler, D.B. Syme, N. Watkins, Nucl.Instrum.Methods A, **329** (1993) 277 290.

[2]. O. N. Jarvis, J. M. Adams, F.B. Marcus, G. J. Sadler, Fusion Eng.Design, **34-35** (1997) 59 66.

[3]. G. Bonheure, M.Angelone, R.Barnsley, L.Bertalot, S.Conroy, G.Ericsson, B.Esposito, J.Kaellne, M.Loughlin, A.Murari, J.Mlynar, M.Pillon, S.Popovichev, B.Syme, M.Tardocchi, M. Tsalas, Proc. of Science FNDA, S. 091, 2006.

[4]. R.S. Granetz, P. Smeulders, Nuclear fusion, **28** (1988) 457 476]

[5]. L.C. Ingesson, B. Alper, H. Chen, A.W. Edwards, G.C. Fehmers, J.C. Fuchs, R. Giannella, R.D. Gill, L. Lauro-Taroni, M. Romanelli, Nucl. Fusion **38** (1998) 167]

[6]. M. J. Mantsinen, L.C. Ingesson, T. Johnson, V.G. Kiptily, M.-L. Mayoral, S. E. Sharapov, B. Alper, L. Bertalot, Phys. Rev. Lett. **89** (2002) 115004-1-4.

[7]. V.G. Kiptily, F.E. Cecil, O.N. Jarvis, M.J. Mantsinen, S.E. Sharapov, L. Bertalot, S. Conroy, L.C. Ingesson, T. Johnson, K.D. Lawson, S. Popovichev, Nucl. Fusion **42** (2002) 999 1007.

[8]. V.G. Kiptily, J.M. Adams, L. Bertalot, A. Murari, S.E. Sharapov, V. Yavorskij, B. Alper, R. Barnsley, P. de Vries, C. Gowers, L.-G. Eriksson, P.J. Lomas, M.J. Mantsinen, A. Meigs, J.-M. Noterdaeme, F.P. Orsitto, Nucl. Fusion **45** (2005) L21–L25.

[9]. D. Stork, Yu. Baranov, P. Belo, L. Bertalot, D. Borba, J.H. Brzozowski, C.D. Challis, D. Ciric, S. Conroy, M. de Baar, P. de Vries, P. Dumortier, L. Garzotti, N.C. Hawkes, T.C. Hender, E. Joffrin T.T.C. Jones, V. Kiptily, P. Lamalle, J. Mailloux, M. Mantsinen, D.C. McDonald, M.F.F. Nave, R. Neu, M. O'Mullane, J. Ongena, R.J. Pearce, S. Popovichev, S.E. Sharapov, M. Stamp, J. Stober, E. Surrey, M. Valovic, I. Voitsekhovitch, H. Weisen, A.D. Whiteford, L. Worth, V. Yavorskij, K.-D. Zastrow, Nucl. Fusion **45** (2005) S181–S194.

[10]. N.C. Hawkes, V.A. Yavorskij, J.M. Adams, Yu F. Baranov, L. Bertalot, C.D. Challis, S. Conroy, V. Goloborod'ko, V. Kiptily, S. Popovichev, K. Schoepf, S.E. Sharapov, D. Stork, E. Surrey, Plasma Phys. Control. Fusion **47** (2005) 1475 1493.

[11]. K.D. Zastrow, J.M. Adams, Yu Baranov, P. Belo, L. Bertalot, J.H. Brzozowski, C.D. Challis, S. Conroy, M. de Baar, P. de Vries, P. Dumortier, J. Ferreira, L. Garzotti, T.C. Hender, E. Joffrin, V. Kiptily, J. Mailloux, D.C. McDonald, R. Neu, M. O'Mullane, M.F.F. Nave, J. Ongena, S. Popovichev, M. Stamp, J. Stober, D. Stork, I. Voitsekhovitch, M. Valovic, H. Weisen, A.D. Whiteford, A. Zabolotsky, Plasma Phys. Control. Fusion **46** (2004) B255 B265.

[12]. P.U. Lamalle, M.J. Mantsinen, J.-M. Noterdaeme, B. Alper, P. Beaumont, L. Bertalot, T. Blackman, Vl.V. Bobkov, G. Bonheure, J. Brzozowski, C. Castaldo, S. Conroy, M. de Baar, E. de la Luna, P. de Vries, F. Durodié, G. Ericsson, L.-G. Eriksson, C. Gowers, R. Felton, J. Heikkinen, T. Hellsten, V. Kiptily, K. Lawson, M. LaxÂback, E. Lerche, P. Lomas, A. Lyssoivan, M.-L. Mayoral, F. Meo, M. Mironov, I. Monakhov, I. Nunes, G. Piazza, S. Popovichev, A. Salmi, M.I.K. Santala, S. Sharapov, T. Tala, M. Tardocchi, D. Van Eester, B. Weyssow, Nucl. Fusion **46** (2006) 391 400.

[13]. M. Anton, H. Weisen, M.J. Dutch, W. von der Linden, F. Buhlmann, R. Chavan, B. Marletaz, P. Marmillod and P. Paris, Plasma Phys. Control. Fusion 38, 1849–1878. (1996)

[14]. G. Bonheure, J. Mlynar, L. Bertalot, S. Conroy, A. Murari, S. Popovichev, L. Zabeo, *32nd* EPS Conference on Plasma Phys. Tarragona, 27 June - 1 July 2005 ECA Vol. 29C, P-1.083 (2005)

[15]. G. Bonheure, S. Popovichev, L. Bertalot, A. Murari, S. Conroy, J. Mlynar, I. Voitsekhovitch, Nucl. Fusion **46** (2006) 725–740

[16]. T. Craciunescu, G. Bonheure, V. Kiptily, A. Murari, S. Soare, I. Tiseanu, V. Zoita, Nuclear Inst. and Methods in Physics Research, A, **595**, p. 623–630, (2008).

[17]. E.T. Jaynes, Proc. IEEE **70** (1982) 939-952.

[18]. B.R. Frieden, J. Opt. Soc. Am. **62**(1972) 511.

[19]. S.F. Gull, J. Skilling, Maximum entropy method in image processing, IEEE Proc .F131 (1984) 646.

[20]. G. Minerbo, Comput. Graphics Image Process. **10** (1979) 48-68.
[21]. A.K. Chattopadhyay, C.V.S. Rao, Review Of Scientific Instruments 76, 063502 (2005).
[22]. J. Kim, W. Choe, Review of Scientific Instruments **77**, 023506-1-6, 2006.
[23]. K. Ertl, W. von der Linden, V. Dose, A. Weller, Nuclear Fusion, Vol. **36**, No. 11 (1996).
[24]. J.-S. Y. D.-C. Seo, and H.-K. Na, Review of Scientific Instruments **76**, 013502 (2005).
[25]. N. Iwama, H. Yoshida, H. Takimoto, Y. Shen, S. Takamura, and T. Tsukishima, Appl. Phys. Lett. **54**, 502-504, 1989.]
[26]. T. Craciunescu, C. Niculae, Gh. Mateescu, C. Turcanu, Journal of Nuclear Materials, **224**, pp. 199-206, 1995.
[27]. I. Tiseanu, T. Craciunescu, Nuclear Science and Engineering, **122**, pp. 384-394, 1996.
[28]. L.A. Shepp, Y. Vardi, IEEE Transactions on Medical Imaging, Vol. **1** (1982) 113 121.
[29]. K. Lange, R. Carson, JCAT vol. **8** (1984) 306-316.
[30]. J. Skilling, in: P.F. Fougère (Ed.), Maximum Entropy and Bayesian Methods, Kluwer Academic Publishers, Dordrecht (1990) pp. 341 350.
[31]. K. Ertl, W. von der Linden, V. Dose, A. Weller, Nuclear Fusion, **36** (1996) 1477 1488.
[32]. A. N. Tikhonov & V. Y. Arsenin, *Solutions of Ill-Posed Problems*, Winston & Sons, Washington, D.C., 1977.
[33]. P. Hansen, Numer. Algo. **46** (2007), pp. 189-194.
[34]. P. C. Hansen, BIT **30** (1990), 658-672.
[35]. G.H. Golub, H. Heath, G. Wahba, Technometrics, **21**(1979)215-223.
[36]. C. L. Lawson & R. J. Hanson, *Solving Least Squares Problems*, Prentice-Hall, Englewood Cliffs, 1974.
[37]. P. C. Hansen, SIAM Review **34** (1992), 561-580.
[38]. V. A. Morozov, Methods for Solving Incorrectly Posed Problems, Springer Verlag, New York, 1984.

Phantom	**Reconstruction method**			
	ML	**ME**	**TR**	**MCBP**
peak	0.993	0.990	0.989	0.996
hollow	0.961	0.949	0.951	0.870
“banana”	0.935	0.931	0.908	0.857
symmetrically reversed “banana”	0.875	0.861	0.836	0.832
peak plus “banana”	0.874	0.667	0.837	0.844

Table 1: The correlation coefficient corr.

Phantom	Reconstruction method			
	ML	ME	TR	MCBP
peak	1.07	1.27	0.98	1.01
hollow	1.23	1.28	1.05	2.05
"banana"	1.30	1.56	1.64	1.85
symmetrically reversed "banana"	1.45	1.59	1.76	1.93
peak plus "banana"	0.86	0.75	1.44	1.86

Table 2: The ratio of reconstructed volumes R_{emiss}.

FIGURE OF MERIT	METHOD	PHANTOM				
		peak	hollow	"banana"	symmetrically reversed "banana"	plus peak "banana"
Horizontal profile	ML	0.07	0.13	0.12	0.17	0.10
	ME	0.11	0.15	0.10	0.28	0.31
	TR	0.05	0.13	0.10	0.22	0.22
	MCBP	0.06	0.22	0.22	0.34	0.25
Vertical profile	ML	0.01	0.10	0.12	0.16	0.19
	ME	0.14	0.14	0.20	0.32	0.23
	TR	0.04	0.23	0.16	0.28	0.18
	MCBP	0.03	0.34	0.26	0.45	0.25
Contour line integral	ML	0.08	0.05	0.14	0.14	0.03
	ME	0.07	0.17	0.33	0.40	0.14
	TR	0.04	0.14	0.20	0.32	0.18
	MCBP	0.20	0.30	0.34	0.47	0.27
Projection	ML	0.04	0.08	0.11	0.11	0.06
	ME	0.08	0.09	0.12	0.12	0.15
	TR	0.09	0.09	0.11	0.15	0.12
	MCBP	0.03	0.16	0.14	0.17	0.11

Tabel 3: Root mean square for figures of merit.

Method	Reconstruction Time (min)
ML	3.5
ME	8 – 12
TR	0.8
MCBP	6

Table 4: Computer time needed for reconstruction.

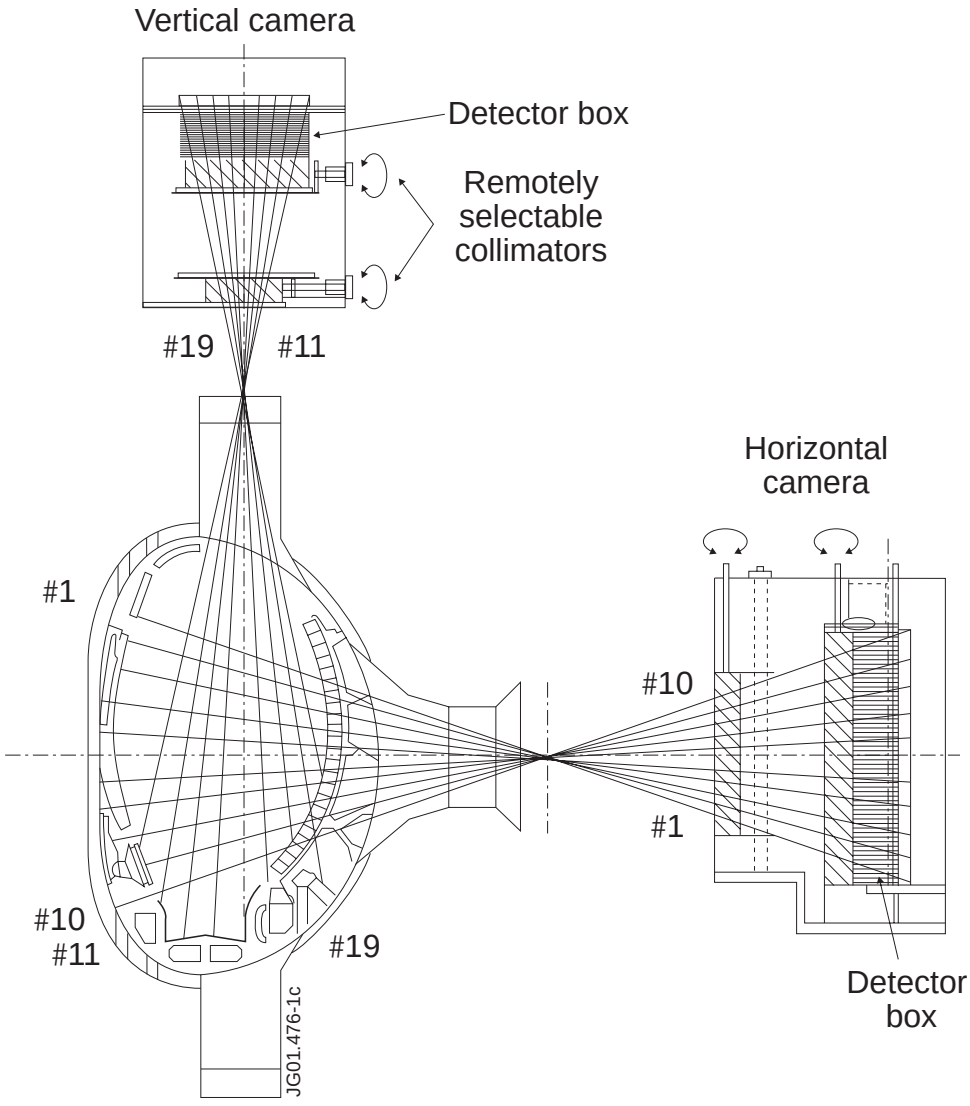

Figure 1: Schematic view of the JET neutron emission profile monitor showing the lines of sight.

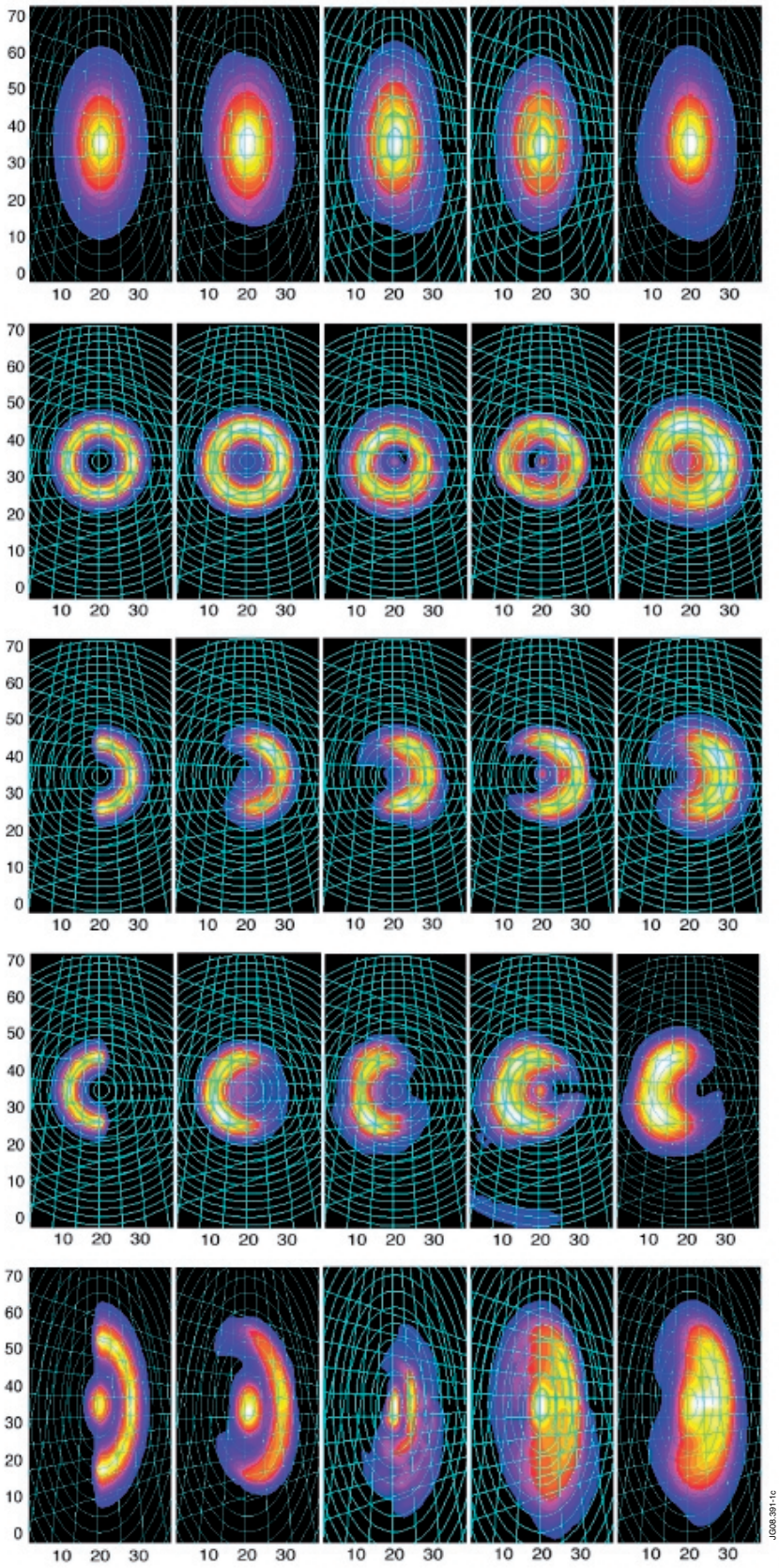

Figure 2: The test phantoms and their reconstruction. Each row corresponds to a phantom - from top to bottom: peak, hollow, "banana", symmetrically reversed "banana" and peak plus "banana". The first column corresponds to the phantom image, the other columns corresponds to reconstructions obtained using the different methods used in this paper – from left to right: ML, ME, TR, MCBP.

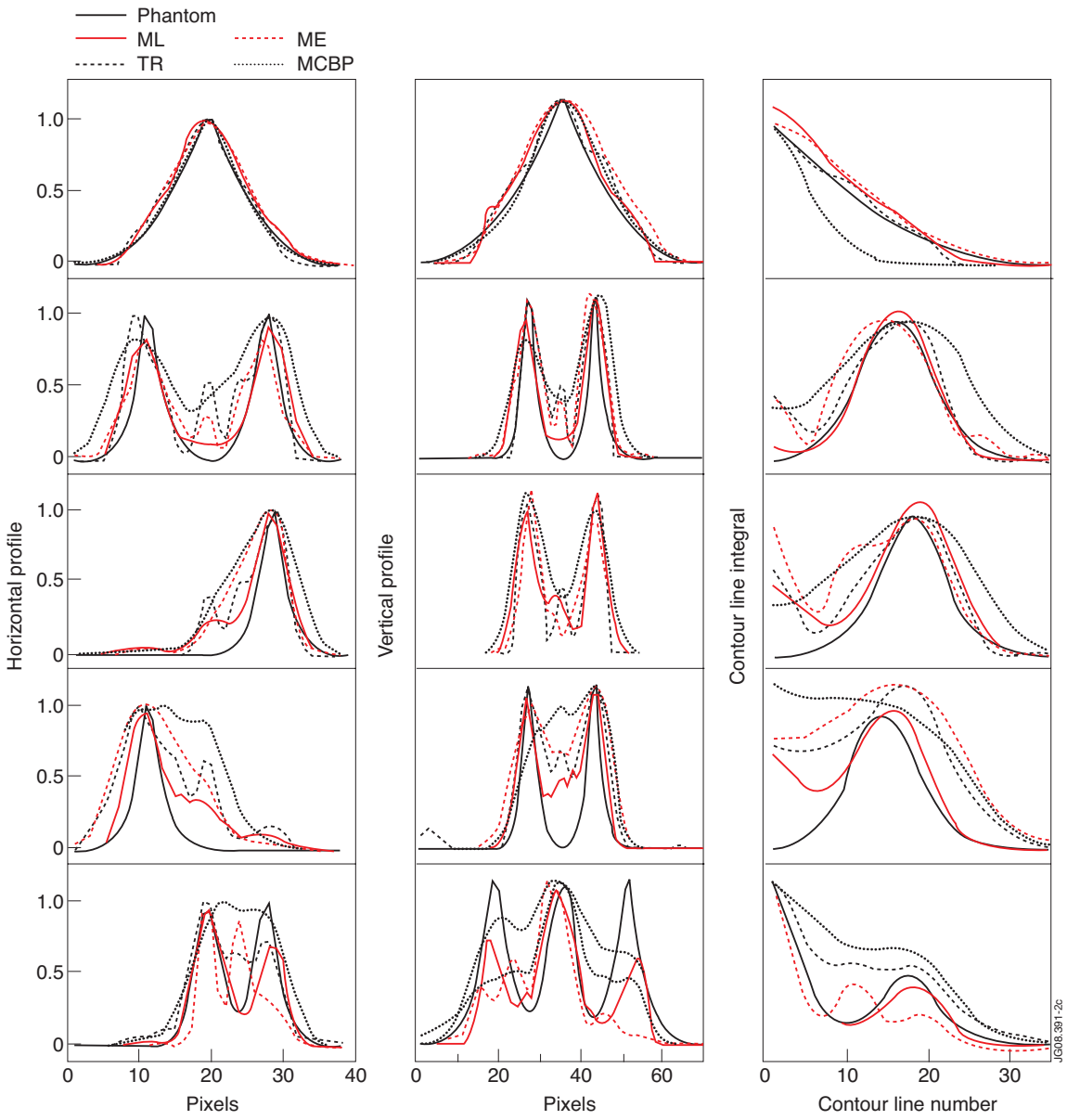

Figure 3: Figures of merit; each row corresponds to a phantom – from top to bottom: peak, hollow, "banana", symmetrically reversed "banana", peak plus "banana"; each column corresponds to a specific figure of merit – from left to right: horizontal line profile, vertical line profile, integrals along magnetic contour lines.

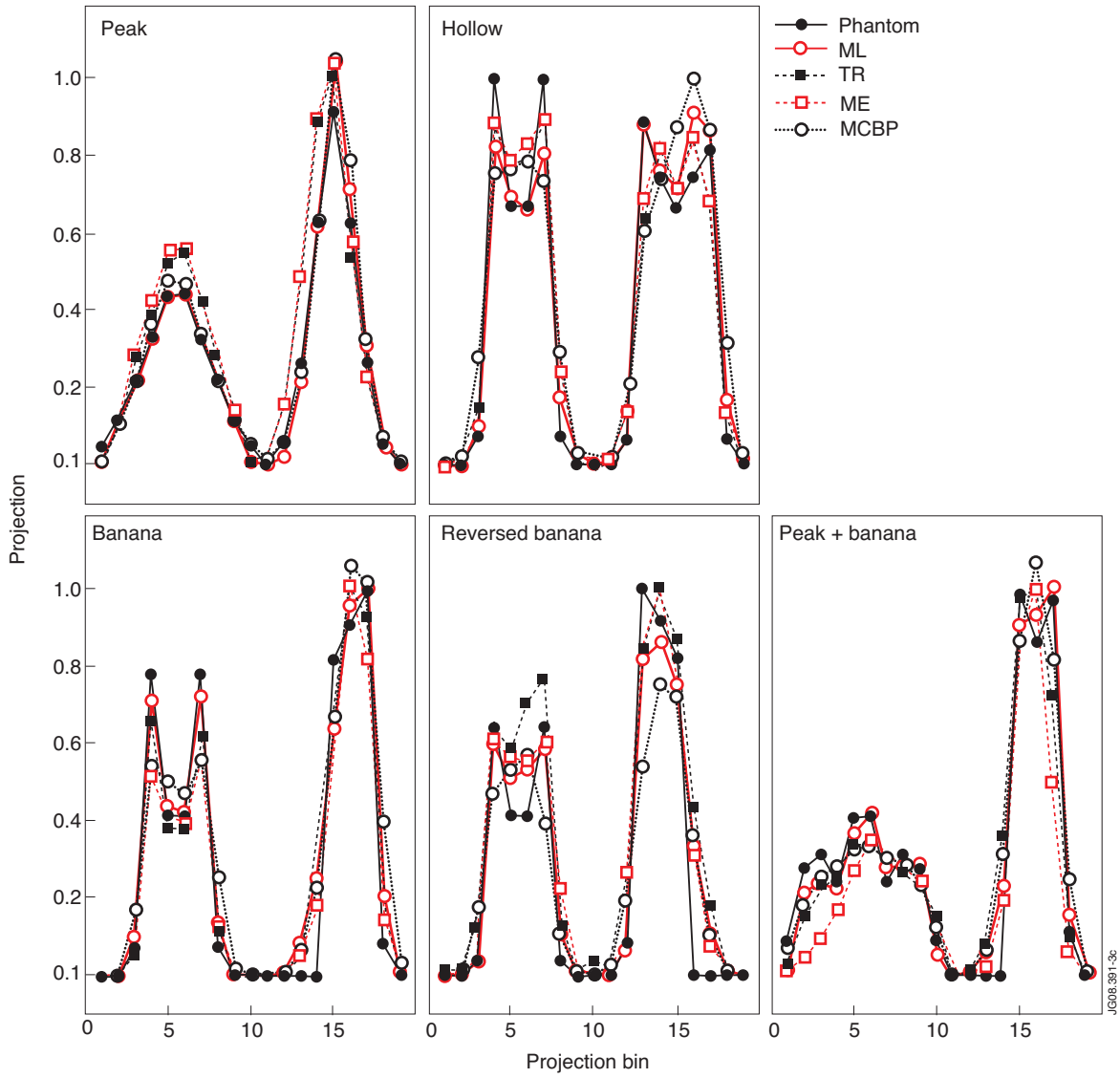

Figure 4: Projections calculated using the phantom and the reconstruction, respectively: peak (top-left), hollow (top-right), "banana" (bottom-left), symmetrically reversed "banana" (bottom-middle), peak plus "banana" (bottom-right).